Available online at www.sciencedirect.com
SCIENCE DIRECT
Journal of Computational Physics 214 (2006) 187–208
JOURNAL OF COMPUTATIONAL PHYSICS
www.elsevier.com/locate/jcp

Surface evolution of elastically stressed films under deposition by a diffuse interface model

Andreas Rätz, Angel Ribalta, Axel Voigt *

Crystal Growth Group, Research Center caesar, Ludwig-Erhard-Allee 2, 53175 Bonn, Germany

Received 24 March 2005; received in revised form 7 September 2005; accepted 16 September 2005
Available online 8 November 2005

Abstract

We consider the heteroepitaxial growth of thin films by numerical simulations within a diffuse interface model. The model is applicable to describe the self-organization of nanostructures. The influence of strain, surface energies and kinetics on the surface evolution is considered. A matched asymptotic analysis shows the formal convergence of an anisotropic viscous Cahn–Hilliard model to a general surface evolution equation. The system is solved by adaptive finite elements in three dimensions and in special cases compared with sharp interface models.

Keywords: Surface evolution; Diffuse interface models; Anisotropy; Adaptive finite elements

1. Introduction

Self-organized semiconductor nanostructures are a promising inexpensive and effective approach to manufacture novel electronic devices. The phenomena of self-organization of nanostructures have been an area of extensive experimental and theoretical research over the past several years. However, producing such quantum-dot-based devices is still challenging. A fundamental understanding of the self-organization process during epitaxial growth therefore could help to produce large numbers of spatially ordered nanostructures with narrow size distribution. In order to understand the nucleation, growth and coarsening phenomena in heteroepitaxial growth, the influence of strain, surface energies and kinetics on the surface evolution has to be considered. These lead to several modeling and numerical issues which have to be taken into account, before simulations can describe the self-organization process.

Strain driven instabilities of a flat surface have been reported for isotropic surface energies by Asaro and Tiller [1], Grinfeld [2] and Srolovitz [3]. This surface instability is a consequence of the competition between strain energy stored in the film and surface energy. Gao and Nix [4] first used this approach to describe the breakup of an unstable film into islands. The growth mode related to this breakup is often refered as

* Corresponding author.
E-mail address: voigt@caesar.de (A. Voigt).

0021-9991/$ - see front matter
doi:10.1016/j.jcp.2005.09.013

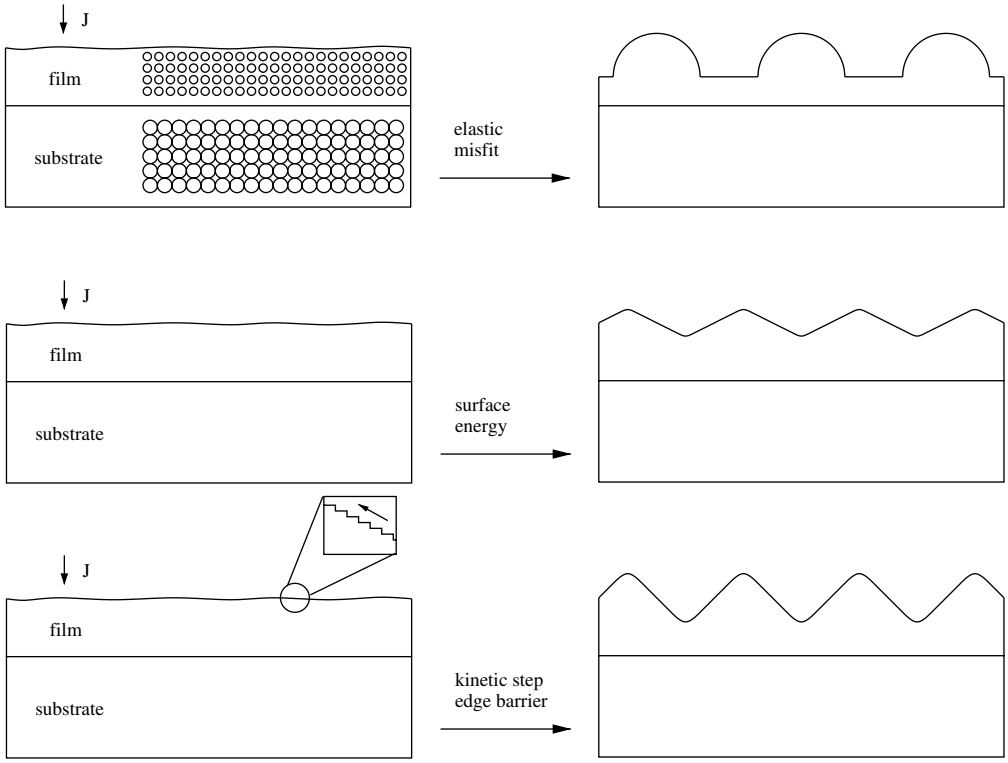

Fig. 1. Schematic description of surface evolution due to elastic misfit including a deposition flux J (top), strong anisotropy in surface energy (middle) and kinetic fluxes (bottom).

Stranski–Krastanov growth. In heteroepitaxial growth the strain in the film results from a mismatch in lattice parameters between film and substrate, see Fig. 1(top).

In addition to the influence of strain there is strong evidence that anisotropic surface energies play a crucial role in heteroepitaxial growth [5]. The formation of nanostructures can result from a thermodynamic instability due to spinodal decomposition into faceted structures with stable orientations [6–12]. This faceting of crystal surfaces is caused by strongly anisotropic surface energies, see Fig. 1(middle). In a continuum framework the corresponding evolution equations to describe the surface evolution with such anisotropic functions are ill posed unless an additional energy of edges and corners is introduced. This leads to curvature dependent surface energies and have been discussed in [13].

For certain materials also anisotropic surface fluxes due to step edge barriers can be responsible for the formation of three-dimensional islands, see Fig. 1(bottom). Villain [14] pointed out that such barriers can give rise to instabilities and lead to pyramidal structures. Siegert and Plischke [15] for example derive a theory which selects the slope of these pyramidal structures by the crystalline symmetry of the growing film.

Approaches towards a continuum description including some of these phenomena derived from a step flow perspective have been performed by [16–19] for example. However their approaches are restricted to $1+1$ dimensions and only consider uniform step trains. We will follow a different ansatz from a rational mechanics perspective as recently proposed by Fried and Gurtin [20]. A direct numerical treatment of the equations seems today not feasible. Several aspects however have already been addressed by numerical simulations in [21–23] using sharp interface methods. We will consider a phase-field description which will allow to overcome some of the numerical difficulties and opens the possibility to add more and more of the relevant phenomena in a consistent way. We consider a viscous Cahn–Hilliard model introduced by Cahn and Taylor [24] and add a deposition flux, elastic misfit strain, anisotropy in the surface free energy density and anisotropy in the kinetic coefficient.

In Section 2, we will start with reviewing the connection between surface motion laws and their diffuse interface approximations for isotropic and anisotropic situations, show how elastic effects and deposition flux can be incorporated and discuss the formation of wetting layers and the incorporation of further phenomena, like phase separation and intermixing. In Section 3, we discuss an adaptive finite element discretization of the model in detail. Finally in Section 4, we show numerical results of the strain driven instability in growing films and compare the simulations with results from sharp interface models. The influence of anisotropy in the surface free energy and kinetic coefficient is discussed and three-dimensional simulations are performed, which show the formation of nanostructures. In Appendix A, we provide a matched asymptotic analysis for anisotropic surface evolution in two dimensions.

2. Continuum modeling of nanoscale surface evolution

Though the basic growth laws have been known from Mullins work [25], who derived them in the context of thermal grooving, strong interest in surface motion has only been initiated recently by the growth of nanostructures. We discuss a continuum model for surface evolution derived from a rational mechanics point of view and relate the sharp interface models to its diffuse interface analogs.

2.1. Surface motion by surface diffusion

We consider the evolution of a $d-1$-dimensional surface $\Gamma = \Gamma(t)$ embedded in $\mathbb{R}^d$ representing the interface between the vapor and a thin film. A growth law for the motion of the surface Γ that combines surface diffusion and interface kinetics was introduced by Cahn and Taylor [24]. In the isotropic situation the equation reads

$$v = -\Delta_s \left(\frac{1}{M} \Delta_s - \frac{1}{D} \right)^{-1} K_{\psi_0} \tag{2.1}$$

with v the normal velocity, $K_{\psi_0} = \psi_0 K = \psi_0 \sum_{i=1}^{d-1} \kappa_i$ the weighted mean curvature including an isotropic surface free energy density ψ_0 and the principal curvatures κ_i and using the convention that an interface given by the graph of a convex function has negative curvature. Furthermore M denotes a positive kinetic coefficient, D a positive diffusion coefficient and Δ_s the surface Laplacian. Two extreme cases of this equation can be considered. In the limit of infinitely fast attachment kinetics ($M = \infty$, D bounded) the equation reduces to

$$v = D \Delta_s K_{\psi_0}, \tag{2.2}$$

whereas for infinitely fast surface diffusion ($D = \infty$, M bounded) we get

$$\frac{1}{M} v = -K_{\psi_0} + c \tag{2.3}$$

with the constant c chosen to fulfill conservation of volume. Eqs. (2.2) and (2.3) are known as motion by surface diffusion and motion by the difference of mean curvature and average mean curvature, respectively. In both cases, volume is preserved and the only driving force for surface motion is surface energy reduction. However, in most applications in modern materials science both growth mechanisms are involved, but numerical studies of the combined model (2.1) do not exist. We can rewrite Eq. (2.1) as a system of two second order equations:

$$v = D \Delta_s w, \tag{2.4}$$

$$w = K_{\psi_0} + \frac{1}{M} v \tag{2.5}$$

with the chemical potential w being the second unknown. In this form the model consists of an equation which follows from the balance of configurational forces and momenta (2.4) and an equation related to mass balance (2.5) and is in agreement with the general framework for interface evolution summarized by Fried and Gurtin [20]. Furthermore, the system (2.4) and (2.5) can be recognized as the sharp interface limit of a diffuse interface approximation, which is based on the introduction of a phase-field function ϕ obtained by smearing out the

discrete function being zero in the vapor and one in the film on a length of ϵ. This diffuse interface approximation of (2.4) and (2.5) is given by a viscous Cahn–Hilliard equation:

$$\partial_t \phi = D\nabla \cdot (\epsilon^{-1} B(\phi)\nabla w), \tag{2.6}$$

$$g(\phi)w = \psi_0(-\epsilon\Delta\phi + \epsilon^{-1}G'(\phi)) + \epsilon\frac{1}{M}\partial_t\phi \tag{2.7}$$

with mobility function $B(\phi) = 36\phi^2(1-\phi)^2$, double well potential $G(\phi) = 18\phi^2(1-\phi)^2$, stabilizing function $g(\phi) = 30\phi^2(1-\phi)^2$. In this context, the interface is given by the levelset

$$\Gamma = \Gamma(t) = \{x \in \Omega : \phi(t,x) = 1/2\}.$$

Cahn, Elliott and Novick-Cohen [26] showed by formal matched asymptotic expansion, that Eqs. (2.6) and (2.7) with $M = \infty$ and $g(\phi) = 1$ reduced for $\epsilon \to 0$ to (2.2). Following their analysis with M bounded yields Eqs. (2.4) and (2.5), as already pointed out in [27]. The function $g(\phi)$ does not change the asymptotic analysis but forces the phase-field variable ϕ to remain within the two phases 0 and 1, see [28].

2.2. Curvature-dependent energy

By extending the evolution equations to the anisotropic situation Eqs. (2.4) and (2.5) read ([24] for example):

$$v = \nabla_s \cdot (D(\mathbf{n})\nabla_s w), \tag{2.8}$$

$$w = \left(\psi_0(\mathbf{n})\mathbf{P} + \frac{\partial^2\psi_0(\mathbf{n})}{\partial\mathbf{n}^2}\right) \cdot \mathbf{L} + \frac{1}{M(\mathbf{n})}v \tag{2.9}$$

with $\mathbf{n}$ the unit normal pointing from the film to the vapor, $M(\mathbf{n})$ an anisotropic positive kinetic coefficient, $D(\mathbf{n})$ an anisotropic positive definite diffusion tensor, $\psi_0(\mathbf{n})$ the anisotropic surface free energy density, $\mathbf{P} = \mathbf{1} - \mathbf{n}\otimes\mathbf{n}$ the projection onto the surface, $\mathbf{L} = -\nabla_s\mathbf{n}$ the curvature tensor and ∇_s the surface gradient. If the surface free energy density ψ_0 is convex the governing equations are well posed. To derive an anisotropic analog of the viscous Cahn–Hilliard model (2.6) and (2.7), we allow the diffusion coefficient D, the mobility function M and the surface free energy density ψ_0 to depend on the normal to the levelset $\phi = 1/2$. Anisotropies in phase-field models have already been discussed. Taylor and Cahn [29] link anisotropic sharp and diffuse surface motion laws via a gradient flow perspective and introduce an appropriate tensor A of rank 2 with the symmetry of the material. The term $\epsilon^2\Delta\phi$ is replaced by $\epsilon^2\nabla\cdot A'(\nabla\phi)$. In [30], the gradient energy coefficient ϵ is allowed to depend on $\mathbf{n}$ and in [31] the mobility function M is chosen anisotropic. As long as the anisotropy in the surface free energy is weak the governing equations read:

$$\partial_t\phi = \nabla\cdot(\tilde{D}(n)\epsilon^{-1}B(\phi)\nabla w), \tag{2.10}$$

$$g(\phi)w = \psi_1(-\epsilon\nabla\cdot(\gamma(n)\nabla\phi + \gamma(n)|\nabla\phi|^2\nabla_{\nabla\phi}\gamma(n)) + \epsilon^{-1}G'(\phi)) + \epsilon\frac{1}{\tilde{M}(n)}\partial_t\phi, \tag{2.11}$$

where the normal is defined by $n = -\nabla\phi/|\nabla\phi|$, the surface free energy density is given by $\psi_0 = \psi_0(n) = \psi_1\gamma(n)$ with a constant ψ_1 and a dimensionless anisotropy function $\gamma = \gamma(n)$. If one chooses the diffusion tensor $\tilde{D}(n) = D(n)/\gamma(n)$ and the kinetic coefficient $\tilde{M}(n) = M(n)/\gamma(n)$, a matched asymptotic analysis which formally shows the convergence of (2.10) and (2.11) to (2.8) and (2.9) for $\epsilon \to 0$ in a two-dimensional setting is given in Appendix A.

If the anisotropy in the surface free energy density is increased the equilibrium shape develops corners and edges whereby certain high energy orientations are excluded from the crystal shape. Thus, for sufficiently large anisotropy, certain orientations are missing resulting in a discontinuous variation in the normal with position along the surface. An analytic criterion to determine the missing orientations on three-dimensional equilibrium shapes was recently given by Sekerka [32]. For such orientations the tensor $\psi_0(\mathbf{n})\mathbf{P} + \frac{\partial^2\psi_0(\mathbf{n})}{\partial\mathbf{n}^2}$ is no longer positive definite and the governing equations become backward parabolic, and hence unstable. One way to deal with such orientations is to allow the interface to contain corners that exclude nonconvex intervals [33]. By using common tangent planes to convexify the $1/\psi_0$-plot and using an appropriately regularized gra-

dient energy coefficient ϵ also the viscous Cahn–Hilliard model (2.10) and (2.11) can be used with such anisotropies to describe corners and facets, as shown numerically in a two-dimensional setting in [34]. However, this ansatz can not characterize the formation of corners or the nucleation of facets, nor can it be used for an initial-value problem in which the initial interface has regions for which $\psi_0(\mathbf{n})\mathbf{P} + \frac{\partial^2\psi_0(\mathbf{n})}{\partial\mathbf{n}^2}$ is not positive definite. In order to study these effects a regularization of Eqs. (2.8) and (2.9) is needed. A possible method is to allow the energy to depend on curvature, thereby penalizing spatial oscillations as well as the tendency to form corners. Such a regularization was first proposed for the dynamic evolution in two dimensions by DiCarlo, Gurtin and Podio-Guidugli [35]. It should be noted that two-dimensional equilibrium shapes should always be smoothly curved at any finite temperature, which follows from general arguments on the absence of long range order in one dimension [36,37]. Therefore, the discussion on missing orientations and their regularization in two dimensions is artificial and should be viewed only as a preliminary study of the three-dimensional case. An extension to three dimensions was given by Gurtin and Jabbour [13]:

$$v = \nabla_s \cdot (D(\mathbf{n})\nabla_s w), \tag{2.12}$$

$$w = \left(\psi_0(\mathbf{n})\mathbf{P} + \frac{\partial^2\psi_0(\mathbf{n})}{\partial\mathbf{n}^2}\right)\cdot\mathbf{L} - \alpha\left(\Delta_s K + K|\mathbf{L}|^2 - \frac{1}{2}K^3\right) + \frac{1}{M(\mathbf{n})}v \tag{2.13}$$

with a positive constant α. The derivation of this model is based on a surface free energy density of the form $\psi(\mathbf{n}, K) = \psi_0(\mathbf{n}) + \frac{1}{2}\alpha K^2$, in which a Willmore-energy is added to the surface free energy in combination with a new lengthscale $\sqrt{\alpha}$ on which sharp corners and edges are smeared out. As a phase-field approximation of Eqs. (2.12) and (2.13), we propose:

$$\partial_t\phi = \nabla\cdot(\tilde{D}(n)\epsilon^{-1}B(\phi)\nabla w), \tag{2.14}$$

$$\begin{aligned} g(\phi)w = {} & \psi_1(-\epsilon\nabla\cdot(\gamma^2(n)\nabla\phi + \gamma(n)|\nabla\phi|^2\nabla_{\nabla\phi}\gamma(n)) + \epsilon^{-1}G'(\phi)) \\ & + \alpha(\Delta(\epsilon\Delta\phi - \epsilon^{-1}G'(\phi)) - (\epsilon\Delta\phi - \epsilon^{-1}G'(\phi))\epsilon^{-2}G''(\phi)) + \epsilon\frac{1}{\tilde{M}(n)}\partial_t\phi. \end{aligned} \tag{2.15}$$

The additional term if compared with Eqs. (2.10) and (2.11) results from a diffuse interface approximation of the Willmore problem introduced in [38]. A formal matched asymptotic analysis showing the convergence for $\epsilon \to 0$ to Eqs. (2.12) and (2.13) is under investigation. The sixth order system in ϕ can be rewritten into a system of three second order equations for ϕ, w and ω, with $\omega = \epsilon\Delta\phi - \epsilon^{-1}G'(\phi)$.

2.3. Elastically stressed films

An important additional driving force for surface motion is due to reduction of elastic energy in stressed films. The elastic stress results from a mismatch in lattice parameters of the film and the substrate and can lead to an instability. This stress-driven instability was first described by Asaro and Tiller [1] and independently rediscovered by Grinfeld [2] and Srolovitz [3]. If the film is relatively thick, then the behavior is equivalent to that of a stressed, semi-infinite solid. An initially planar surface is unstable and evolves to form a cusped morphology. If the film is relatively thin islands or nanocrystals form on the substrate [21,22,39–41]. Both effects follow from a competing influence of surface and elastic energy. For convenience, we introduce the elastic energy in the isotropic model (2.4) and (2.5). We need to add the elastic energy density Ψ:

$$v = D\Delta_s w, \tag{2.16}$$

$$w = K_{\psi_0} + \frac{1}{M}v + \Psi \tag{2.17}$$

and supplement the evolution law with an elasticity equation in the film

$$\nabla\cdot\sigma = 0 \tag{2.18}$$

for the stress field σ. If we assume that the vapor exerts neither standard nor configurational forces on the film and neglect surface stress, the boundary condition for σ at the surface reads

$$\sigma\cdot\mathbf{n} = 0. \tag{2.19}$$

In order to compute the elastic energy density Ψ we follow Hooke's law. The stress is equal to the elastic stiffness times the strain

$$\sigma_{ij} = \sum_{k=1}^{3}\sum_{l=1}^{3} C_{ijkl}(\varepsilon_{kl} - F_{kl}), \tag{2.20}$$

where C_{ijkl} the stiffness tensor, $\varepsilon_{ij} = \frac{1}{2}(\frac{\partial u_i}{\partial x_j} + \frac{\partial u_j}{\partial x_i})$ the strain tensor, with u the displacement field, and $F_{ij} = F\delta_{ij}$ is the misfit strain tensor, with F the coherency strain and δ_{ij} the Kronecker delta. The elastic energy density Ψ is then defined through

$$\Psi = \frac{1}{2}\sum_{i,j,k,l}(\varepsilon_{ij} - F_{ij})C_{ijkl}(\varepsilon_{kl} - F_{kl})$$

and can be computed from the displacement field. For an elastically isotropic film, Hooke's law takes the form:

$$\begin{aligned} \sigma_{ii} &= 2\mu(\varepsilon_{ii} - F) + \lambda\sum_{k=1}^{3}(\varepsilon_{kk} - F), \\ \sigma_{ij} &= 2\mu\varepsilon_{ij}, \quad i \neq j, \end{aligned} \tag{2.21}$$

with Lamé moduli μ and λ. Substituting (2.20) and using Hooke's law (2.21), the elastic energy density Ψ can be computed as

$$\Psi = \mu\sum_{i}(\varepsilon_{ii} - F)^2 + 2\mu(\varepsilon_{12}^2 + \varepsilon_{13}^2 + \varepsilon_{23}^2) + \frac{1}{2}\lambda\left(\sum_{i}(\varepsilon_{ii} - F)\right)^2. \tag{2.22}$$

To incorporate the elastic energy in the viscous Cahn–Hilliard model (2.6) and (2.7) we need to add the partial derivative of Ψ with respect to the phase-field variable ϕ:

$$\partial_t\phi = D\nabla\cdot\epsilon^{-1}B(\phi)\nabla w, \tag{2.23}$$

$$g(\phi)w = \psi_0(-\epsilon\psi_0^2\Delta\phi + \epsilon^{-1}G'(\phi)) + \epsilon\frac{1}{M}\partial_t\phi + \Psi'(\phi), \tag{2.24}$$

where $\Psi = \Psi(\phi)$ will be defined in the following. The system is related to the Cahn–Larché system [42]. Similar approaches to incorporate elastic effects into phase-field models have been considered in [43–47]. If we let the stiffness tensor C_{ijkl} (or in the isotropic situation the Lamé moduli λ and μ) and the coherency strain F to depend on the phase-field variable ϕ, we can formulate the elasticity Eq. (2.18) on the whole domain. In the isotropic situation the equation reads for each component $i = 1,2,3$

$$-\nabla\cdot\mu_\phi\nabla u_i - \nabla\cdot\lambda_\phi\sum_j A_{ij}\nabla u_j - \nabla\cdot\mu_\phi\sum_j A_{ji}\nabla u_j = -\frac{\partial}{\partial x_i}((2\mu_\phi + 3\lambda_\phi)F_\phi), \tag{2.25}$$

where A_{ij} is the matrix with one in position ij and zero elsewhere. The elastic energy density Ψ is thus defined through

$$\Psi(\phi) = \mu_\phi\sum_{i}(\varepsilon_{ii} - F_\phi)^2 + 2\mu_\phi(\varepsilon_{12}^2 + \varepsilon_{13}^2 + \varepsilon_{23}^2) + \frac{1}{2}\lambda_\phi\left(\sum_{i}(\varepsilon_{ii} - F_\phi)\right)^2 \tag{2.26}$$

and its derivative with respect to ϕ is

$$\begin{aligned} \Psi'(\phi) = {} & \partial_\phi\mu_\phi\sum_{i}(\varepsilon_{ii} - F_\phi)^2 + 2\partial_\phi\mu_\phi(\varepsilon_{12}^2 + \varepsilon_{13}^2 + \varepsilon_{23}^2) + \frac{1}{2}\partial_\phi\lambda_\phi\left(\sum_{i}(\varepsilon_{ii} - F_\phi)\right)^2 \\ & - (2\mu_\phi + 3\lambda_\phi)\partial_\phi F_\phi\sum_{i}(\varepsilon_{ii} - F_\phi). \end{aligned}$$

The coefficients μ_ϕ, λ_ϕ and F_ϕ are given by

$$\mu_\phi = \mu h(\phi) + \mu^v, \quad \lambda_\phi = \lambda h(\phi), \quad F_\phi = F h(\phi), \tag{2.27}$$

where μ^v is a small positive value to avoid numerical instabilities that are present when $\mu_\phi(0) = 0$, μ, λ and F the material parameters of the film and $h(\phi)$ such that $h'(\phi) = g(\phi)$.

2.4. Deposition flux

A deposition flux is incorporated into (2.6) and (2.7) by adding $\epsilon^{-1} j$ to Eq. (2.6), with j given by

$$j = -J \cdot n = -J_z n_z = J_z \frac{\partial_z \phi}{|\nabla \phi|} = -VB(\phi)\mathscr{R}\frac{\partial_z \phi}{|\nabla \phi|},$$

where J is the vector valued deposition flux. Furthermore V denotes the constant velocity of a flat interface and $\mathscr{R}$ is a random number in $[1 - R, 1 + R]$, $R \in (0, 1)$, modeling noise. In this form the deposition flux is smeared out over the diffuse interface.

2.5. Wetting layer

In order to simulate the formation of islands or nanocrystals an interaction between substrate and vapor has to be considered. If the film wets the substrate, the formed islands are usually separated by a thin wetting layer. For such a wetting layer to be favored, the surface free energy of the film ψ_0^{f} must be less than that of the substrate ψ_0^{s}. As shown by Spencer [48], the abrupt change in material parameters can be approximated within a boundary-layer model in which the surface free energy is allowed to depend on the film height

$$\psi_0(h) = \psi_0^{\mathrm{f}} + (\psi_0^{\mathrm{s}} - \psi_0^{\mathrm{f}}) \exp(-h/h_0), \tag{2.28}$$

with h_0 the transition layer thickness. If $h \gg h_0$ the surface properties of the film are identical with the bulk properties and are not effected by the substrate, but if $h = 0$ the effective surface free energy corresponds to that of the exposed substrate. However an exposed substrate would result in a larger surface energy and should therefore be prevented. In addition the coherency strain F can be modeled as

$$F(h) = F(1 - \exp(-h/h_0)) \tag{2.29}$$

or another appropriate function leading to a misfit strain F_{ij} when $h \gg h_0$ and zero in the substrate. If the transition layer thickness is in the order of the lattice spacing the boundary layer model is a reasonable continuum approach to describe wetting layers with thickness of a few monolayers.

2.6. Further effects

Besides the described effects further reasons responsible for the formation of islands are assumed to be relevant and should be accounted for in a quantitative simulation of heteroepitaxial growth [20]. One of these sources is surface stress. Shchukin and Bimberg [49] show a strong influence of surface stress on the formation of surface pattern. Furthermore Shenoy and Freund [19] demonstrate the existence of an instability induced solely by surface strain. They used the underlying physics of crystallographic steps to provide a basis for the orientation and strain dependence of the surface energy. Another effect not accounted for is a diffusion path through the bulk and the presence of several species, which can lead to phase separation and inhomogeneities in the film, as numerically studied in [50]. The driving force for these atomic motions is assumed to be strain-enhanced diffusion. Intermixing effects in the wetting layer furthermore might give an explanation for the occurence of relatively thick wetting layers which can not be described with the approach in Section 2.5. Furthermore the presence of adatoms on the surface is not accounted for. Adatoms are important in describing segregation effects at the surface [51,52] and even if only one species is present they are able to provide a diffusion path on flat parts of the surface, where due to the constant curvature surface diffusion would no longer be active. And as already mentioned in Section 1, anisotropic surface fluxes due to step-edge barriers might be responsible for the formation of islands, however how to incorporate this effect in a 3D continuum description is still open.

3. Discretization of a viscous Cahn–Hilliard model for stressed films

Here we describe the numerical approach in the isotropic case and only consider the fourth order system. Modifications in the anisotropic situation are straight foreward and are only briefly addressed in Section 4. The effect of elastic stress due to lattice mismatch on the surface morphology has already been studied numerically within a phase-field approximation in [53,54] in two dimensions with convexified anisotropic surface energies and in the isotropic case by Barrett, Garcke and Nürnberg [55]. Neither of these approaches takes into account the kinetic coefficient M.

We solve the system in a cubic domain $\Omega \subset \mathbb{R}^3$. On the top of the cube the boundary conditions are prescribed by $\phi = w = 0$ and null flux for the displacement. The boundary between film and substrate are null flux for ϕ and w and $u_i = 0$, which is the natural condition if we have a rigid substrate. The remaining parts are assumed to be periodic, see Fig. 2.

The system is solved by an operator splitting ansatz, thereby in each timestep the derivative of the elastic energy density serves as a given quantity in the computation for the phase-field variable ϕ and the chemical potential w, whereas the phase-field variable serves as a given parameter in computing the displacement field. The algorithm is implemented in AMDiS, an adaptive finite element toolbox for scientific computing, [56,57].

3.1. Numerical computation of phase-field and chemical potential

The time interval is split by discrete time instants $0 = t_0 < t_1 < \cdots$, from which one gets the time steps $\Delta t_m := t_{m+1} - t_m$, $m = 0, 1, \ldots$ The derivative of the doublewell potential is linearized by

$$G'(\phi^{(m+1)}) \approx G'(\phi^{(m)}) + G''(\phi^{(m)})(\phi^{(m+1)} - \phi^{(m)}) = G''(\phi^{(m)})\phi^{(m+1)} + G'(\phi^{(m)}) - G''(\phi^{(m)})\phi^{(m)}.$$

Using this time discretization one ends up with the weak formulation

$$\begin{aligned}
&\frac{1}{\Delta t_m}\int_\Omega \phi^{(m+1)}\psi + \epsilon^{-1}\int_\Omega DB(\phi^{(m)})\nabla w^{(m+1)}\cdot\nabla\psi \\
&\quad = \frac{1}{\Delta t_m}\int_\Omega \phi^{(m)}\psi + \epsilon^{-1}\int_\Omega j(\phi^{(m)},\nabla\phi^{(m)})\psi \int_\Omega g(\phi^{(m)})w^{(m+1)}\psi \\
&\qquad - \epsilon\psi_0\int_\Omega \nabla\phi^{(m+1)}\cdot\nabla\psi - \epsilon^{-1}\psi_0\int_\Omega G''(\phi^{(m)})\phi^{(m+1)}\psi - \frac{\epsilon}{\Delta t_m}\int_\Omega \frac{1}{M}\phi^{(m+1)}\psi \\
&\quad = -\frac{\epsilon}{\Delta t_m}\int_\Omega \frac{1}{M}\phi^{(m)}\psi + \int_\Omega \Psi'(\phi^{(m)})\psi + \epsilon^{-1}\psi_0\int_\Omega (G'(\phi^{(m)}) - G''(\phi^{(m)})\phi^{(m)})\psi
\end{aligned}$$

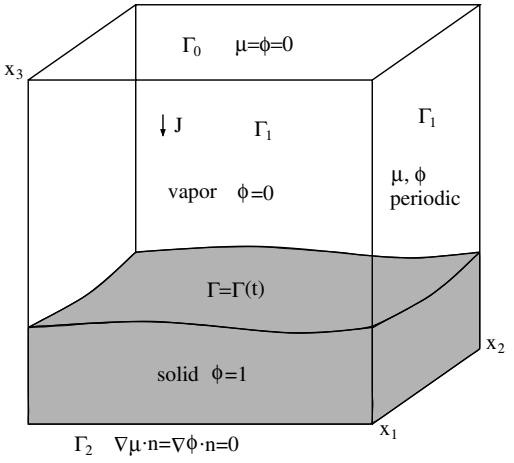

Fig. 2. Computational domain and boundary conditions.

for all $\psi \in X := \{\psi \in H^1(\Omega) : \psi_{|\Gamma_0} = 0, \psi_{|\Gamma_1} \text{periodic}\}$. To discretize in space, let $\mathscr{T}_h^m$ be a conforming triangulation of Ω at time instant t_m. Define the finite element space of globally continuous, piecewise linear elements

$$\mathbb{V}_h^m = \{v_h \in X : v_h|_T \in \mathbb{P}^1 \ \forall T \in \mathscr{T}_h^m\}.$$

The space discretization now reads: find $\phi_h^{(m+1)}, w_h^{(m+1)} \in \mathbb{V}_h^{m+1}$ such that

$$\begin{aligned}
&\frac{1}{\Delta t_m}\int_\Omega \phi_h^{(m+1)}\psi + \epsilon^{-1}\int_\Omega DB(\phi_h^{(m)})\nabla w_h^{(m+1)}\cdot\nabla\psi \\
&\quad = \frac{1}{\Delta t_m}\int_\Omega \phi_h^{(m)}\psi + \epsilon^{-1}\int_\Omega j(\phi_h^{(m)},\nabla\phi_h^{(m)})\psi\int_\Omega g(\phi_h^{(m)})w_h^{(m+1)}\psi \\
&\qquad - \psi_0\epsilon\int_\Omega \nabla\phi_h^{(m+1)}\cdot\nabla\psi - \epsilon^{-1}\psi_0\int_\Omega G''(\phi_h^{(m)})\phi_h^{(m+1)}\psi - \frac{\epsilon}{\Delta t_m}\int_\Omega \frac{1}{M}\phi_h^{(m+1)}\psi \\
&\quad = -\frac{\epsilon}{\Delta t_m}\int_\Omega \frac{1}{M}\phi_h^{(m)}\psi + \int_\Omega \Psi'(\phi_h^{(m)})\psi + \psi_0\epsilon^{-1}\int_\Omega (G'(\phi_h^{(m)}) - G''(\phi_h^{(m)})\phi_h^{(m)}\psi)
\end{aligned}$$

for all $\psi \in \mathbb{V}_h^{m+1}$. These lead to a linear system of equations for $\Phi^{(m+1)}$ and $W^{(m+1)}$, with $\phi_h^{(m+1)} = \sum \Phi_i^{(m+1)}\psi_i$ and $w_h^{(m+1)} = \sum W_i^{(m+1)}\psi_i$:

$$\begin{aligned}
&\frac{1}{\Delta t_m}\boldsymbol{M}^1\Phi^{(m+1)} + \epsilon^{-1}\boldsymbol{A}^1 W^{(m+1)} = \frac{1}{\Delta t_m}\boldsymbol{M}^1\Phi^{(m)} + \epsilon^{-1}\boldsymbol{J}, \\
&\boldsymbol{M}^2 W^{(m+1)} - \epsilon\boldsymbol{A}^2\Phi^{(m+1)} - \epsilon^{-1}\boldsymbol{G}^{\mathrm{i}}\Phi^{(m+1)} - \frac{\epsilon}{\Delta t_m}\boldsymbol{M}^3\Phi^{(m+1)} = -\frac{\epsilon}{\Delta t_m}\boldsymbol{M}^3\Phi^{(m)} + \boldsymbol{F} + \epsilon^{-1}\boldsymbol{G}^{\mathrm{e}}
\end{aligned}$$

with

$$\begin{aligned}
&\boldsymbol{M}^1 = (M^1_{ij}),\ M^1_{ij} = (\psi_i,\psi_j)_\Omega; \quad \boldsymbol{M}^2 = (M^2_{ij}),\ M^2_{ij} = (g(\phi_h^{(m)})\psi_i,\psi_j)_\Omega; \\
&\boldsymbol{M}^3 = (M^3_{ij}),\ M^3_{ij} = \left(\frac{1}{M}\psi_i,\psi_j\right)_\Omega; \quad \boldsymbol{A}^1 = (A^1_{ij}),\ A^1_{ij} = (DB(\phi_h^{(m)}\nabla\psi_i,\nabla\psi_j)_\Omega; \\
&\boldsymbol{A}^2 = (A^2_{ij}),\ A^2_{ij} = (\psi_0\nabla\psi_i,\nabla\psi_j)_\Omega; \quad \boldsymbol{J} = (J_i),\ J_i = (j(\phi_h^{(m)},\nabla\phi_h^{(m)}),\psi_i)_\Omega; \\
&\boldsymbol{F} = (F_i),\ F_i = \Psi'(\phi_h^{(m)}),\psi_i)_\Omega; \quad \boldsymbol{G}^{\mathrm{i}} = (G^{\mathrm{i}}_{ij}),\ G^{\mathrm{i}}_{ij} = (\psi_0 G''(\phi_h^{(m)})\psi_i,\psi_j)_\Omega; \\
&\boldsymbol{G}^{\mathrm{e}} = (G^{\mathrm{e}}_i),\ G^{\mathrm{e}}_i = \psi_0(G'(\phi_h^{(m)}) - G''(\phi_h^{(m)})\phi_h^{(m)},\psi_i)_\Omega,
\end{aligned}$$

where $(\cdot,\cdot)_\Omega$ denotes the L^2 scalar product. Thus, written in block-matrix-form the linear system

$$\begin{pmatrix} \epsilon^{-1}\boldsymbol{A}^1 & \frac{1}{\Delta t_m}\boldsymbol{M}^1 \\ \boldsymbol{M}^2 & -\epsilon\boldsymbol{A}^2 - \epsilon^{-1}\boldsymbol{G}^{\mathrm{i}} - \frac{\epsilon}{\Delta t_m}\boldsymbol{M}^3 \end{pmatrix}\begin{pmatrix} W^{(m+1)} \\ \Phi^{(m+1)} \end{pmatrix} = \begin{pmatrix} \frac{1}{\Delta t_m}\boldsymbol{M}^1\Phi^{(m)} + \epsilon^{-1}\boldsymbol{J} \\ -\frac{\epsilon}{\Delta t_m}\boldsymbol{M}\Phi^{(m)} + \boldsymbol{F} - \epsilon^{-1}\boldsymbol{G}^{\mathrm{e}} \end{pmatrix}$$

has to be solved in every timestep. The system is not symmetric and is iteratively solved by a stabilized biconjugate gradient method (BiCGStab).

3.2. Numerical computation of displacement and energy density

The numerical solution of the elasticity problem (2.25) using finite elements is standard. Multiplying (2.25) by a test function $\psi \in Y$, where $Y := \{\psi \in H^1(\Omega) : \psi_{|\Gamma_2} = 0, \psi_{|\Gamma_1} \text{periodic}\}$, with Γ_2 the Dirichlet boundary and Γ_1 the periodic boundary of the domain Ω, and integrating by parts yields

$$\int_\Omega \mu_\phi \nabla u_i\nabla\psi + \int_\Omega \lambda_\phi \sum_j A_{ij}\nabla u_j\cdot\nabla\psi + \int_\Omega \mu_\phi\sum_j A_{ji}\nabla u_j\cdot\nabla\psi = -\int_\Omega (2\mu_\phi + 3\lambda_\phi)F_\phi\frac{\partial\psi}{\partial x_i}$$

for $i = 1,2,3$. The space discretization now reads: find $u_{i,h} \in \mathbb{W}_h^m$, with

$$\mathbb{W}_h^m = \{v_h \in Y : v_h|_T \in \mathbb{P}^1 \ \forall T \in \mathscr{T}_h^m\}.$$

such that for all $\psi \in \mathbb{V}_h^m$

$$\int_\Omega \mu_\phi \nabla u_{i,h} \cdot \nabla \psi + \int_\Omega \lambda_\phi \sum_j A_{ij} \nabla u_{j,h} \cdot \nabla \psi + \int_\Omega \mu_\phi \sum_j A_{ji} \nabla u_{j,h} \cdot \nabla \psi = -\int_\Omega (2\mu_\phi + 3\lambda_\phi) F_\phi \frac{\partial \psi}{\partial x_i}$$

for $i = 1,2,3$. This leads to the following symmetric positive definite system of equations for U_i with $u_{i,h} = \sum U_{i,k}\psi_k$, which we iteratively solve using the conjugate gradient method (CG).

$$\begin{pmatrix} \mathbf{A}_{11} & \mathbf{A}_{12} & \mathbf{A}_{13} \\ \mathbf{A}_{21} & \mathbf{A}_{22} & \mathbf{A}_{23} \\ \mathbf{A}_{31} & \mathbf{A}_{32} & \mathbf{A}_{33} \end{pmatrix} \begin{pmatrix} U_1 \\ U_2 \\ U_3 \end{pmatrix} = \begin{pmatrix} f_1 \\ f_2 \\ f_3 \end{pmatrix},$$

where

$$(\mathbf{A}_{ii})_{kl} = \int_\Omega (2\mu_\phi + \lambda_\phi) \frac{\partial \psi_l}{\partial x_i} \frac{\partial \psi_k}{\partial x_i} + \mu_\phi \sum_{j \neq i} \frac{\partial \psi_l}{\partial x_j} \frac{\partial \psi_k}{\partial x_j},$$

$$(\mathbf{A}_{ij})_{kl} = \int_\Omega \mu_\phi \frac{\partial \psi_l}{\partial x_i} \frac{\partial \psi_k}{\partial x_j} + \lambda_\phi \frac{\partial \psi_l}{\partial x_j} \frac{\partial \psi_k}{\partial x_i}, \qquad i \neq j,$$

$$(f_i)_k = -2F(2\mu + 3\lambda) \int_\Omega g(\phi) g'(\phi) \frac{\partial \phi}{\partial x_i} \psi_k.$$

For computing the elastic energy density the gradient of the displacement field is needed. We use a recovery technique based on averaging of the gradient of the computed solution to obtain a continuous approximation of the gradient. To be precise, for each vertex x of the finite element mesh, let

$$T_x = \cup_{x \in T} T$$

be the union of all elements of the partition that contain x as a vertex. The value of the recovered gradient at vertex x is given by

$$G u_{i,h}(x) = \sum_{T \in T_x} \frac{|T|}{|T_x|} \nabla u_{i,h}|_T.$$

Here, $G\, u_{i,h}$ is the recovered gradient, and $|T|, |T_x|$ denote the volume of T and T_x.

3.3. Adaptive strategy of local refinement and coarsening

To obtain satisfactory computational results, a mesh with a sufficiently fine resolution near the interface is needed. Noting that a uniform refinement would be prohibitive from the computational point of view, we are naturally led to adopt local mesh refinement and coarsening. At every time step, the finite element mesh from the previous time step is locally refined and/or coarsened according to a L^2-like error indicator for the Cahn–Hilliard equation. For every element T, we define $\eta_T(\phi_h) := (\sum_{e \in \partial T} \int_e h^3 \mid [\frac{\partial \phi_h}{\partial n_e}]|^2)^{1/2}$, where $[\frac{\partial \phi_h}{\partial n_e}]$ denotes the jump of the normal derivative of ϕ_h across an edge $e \subset \partial T$. This can be used to define an indicator for the error $\|\phi - \phi_h\|$ on the whole domain $\eta(\phi_h) := (\sum_{T \in T_\Omega^m} \eta_T^2(\phi_h))^{1/2}$. The criterion for refinement and coarsening is based on an equidistribution strategy, which attempts to enforce $\eta_T(\phi_h) = \eta_{T'}(\phi_h)$ for all $T, T' \in T_\Omega^m$. If this condition were enforced, at least approximately, then we would have $\eta(\phi_h) \approx N_m^{1/2} \eta_T(\phi_h)$, where N_m is the number of elements in T_Ω^m. We thus mark an element $T \in T_\Omega^m$ for refinement and/or coarsening, if $\eta_T(\phi_h) > \frac{\eta(\phi_h)}{N_m^{1/2}}$, $\eta_T(\phi_h) \leqslant \theta \frac{\eta(\phi_h)}{N_m^{1/2}}$, respectively, with some $\theta \in (0,1)$. Even if this strategy is only based on the phase-field variable ϕ the adapted mesh is also used to solve the elasticity problem. The recovered gradient of ϕ is used to estimate the error in the displacement field [58] and verify the used grid. The performed simulations show that no further refinement for the elasticity problem is necessary. However a coarser mesh at the boundary might be possible to obtain the same accuracy.

4. Numerical results

We start by comparing the solution of the viscous Cahn–Hilliard equation with the sharp interface solution for isotropic surface diffusion and volume preserved mean curvature flow with a prescribed elastic energy

density in two dimensions. As a second test case we introduce a weakly anisotropic surface free energy density and a strong anisotropy function in the kinetic coefficient, and analyse the convergence towards the Wulff-shape and the kinetic Wulff-shape, respectively. Here elasticity is neglected. As a final result we couple the viscous Cahn–Hilliard equation with the elasticity problem and solve the overall system with anisotropy in the free energy density and the kinetic coefficient in three dimensions.

4.1. Comparison between phase-field and sharp interface model

In order to demonstrate the validity of the viscous Cahn–Hilliard equation with elasticity we will first compare the numerical solutions with the corresponding sharp interface models in the limits $M \to \infty$ and $D \to \infty$. For these equations and a prescribed elastic energy density the Asaro–Tiller–Grinfeld instability can be used as a test case in two dimensions. In all simulations we keep the parameter $\epsilon = 0.1$. We introduce the evolution equation

$$v = \partial_{ss}(K + \Psi), \tag{4.30}$$

with ∂_s the derivative with respect to the arclength. The elastic energy density Ψ is given by

$$\Psi(x_1, x_2) = -\frac{C}{x_2 - a_2 + r}, \quad a_2 = \inf_{x \in \Omega} x_2, \quad r > 0. \tag{4.31}$$

In the case of a graph formulation (4.30) and (4.31) with $r = 0$ have been considered in [59] in order to study crack formation. The positive number r in (4.31) has a regularizing meaning. We consider the domain $\Omega := (-1,1) \times (-1,1)$ and a perturbation

$$\tilde{\Gamma} := \{(x_1, x_2) \in \Omega : x_2 = -0.05 \cos(\pi x_1)\}$$

of the flat interface

$$\Gamma := \{(x_1, x_2) \in \Omega : x_2 = 0\}.$$

Following the linear stability analysis in [59] one obtains the growth rate

$$\omega(k = 1) = -\pi^4 + \frac{C}{(1+r)^2}\pi^2. \tag{4.32}$$

For the numerical results presented here $C = 50$ and $r = 1/2$ have been used, which yields the growth rate $\omega = \pi^2(\frac{200}{9} - \pi^2) \approx 121.92$.

In Fig. 3 a comparison of a sharp interface simulation of (4.30) with a phase-field simulation of (2.6) and (2.7) with $\psi_0 = 1$, $D = 1$ and $M = 500$ is shown.

For the sharp interface simulations the algorithm in [60] is used. We show the plots of the evolving curve at three different timesteps compared to the levelsets $\phi = 1/2$ at the corresponding timesteps. Fig. 4 shows for one timestep convergence of the levelsets to the sharp interface solution for increasing M. This convergence can also be seen in the plots of the logarithm of the amplitudes versus time in Fig. 5. In order to compute the growthrate linear fits of these plots have been performed to determine the slope (fit-interval: $[0, 0.01]$). The result of this can be seen in Table 1.

As a second example we introduce the evolution law

$$v = (K - \bar{K} - (\Psi - \bar{\Psi})), \tag{4.33}$$

where

$$\bar{K} = \frac{1}{|\Gamma|}\int_\Gamma K \, \mathrm{d}s \quad \text{and} \quad \bar{\Psi} := \frac{1}{|\Gamma|}\int_\Gamma \Psi \, \mathrm{d}s.$$

and Ψ as in (4.31). Similar as in the case of (4.30) linear stability analysis yields the growth rate

$$\omega(k = 1) = -\pi^2 + \frac{C}{(1+r)^2} = -\pi^2 + \frac{50}{2.25} \approx 12.35 \tag{4.34}$$

with C and r as before.

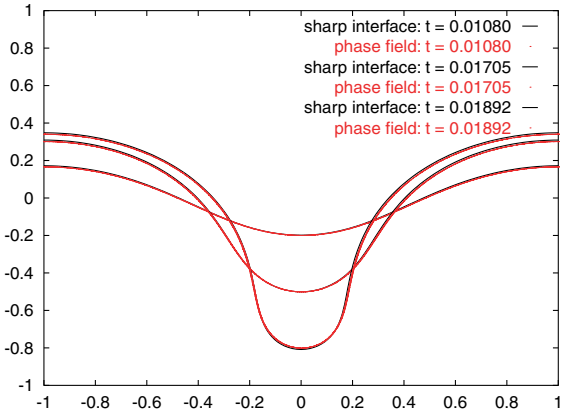

Fig. 3. Sharp interface versus phase-field at various timesteps, $M = 500$.

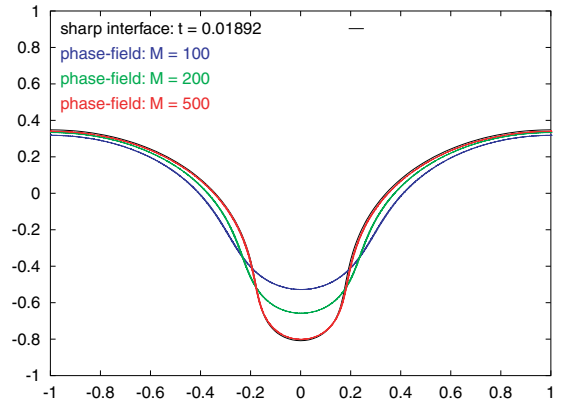

Fig. 4. Convergence of levelsets of phase-field model to sharp interface for increasing M.

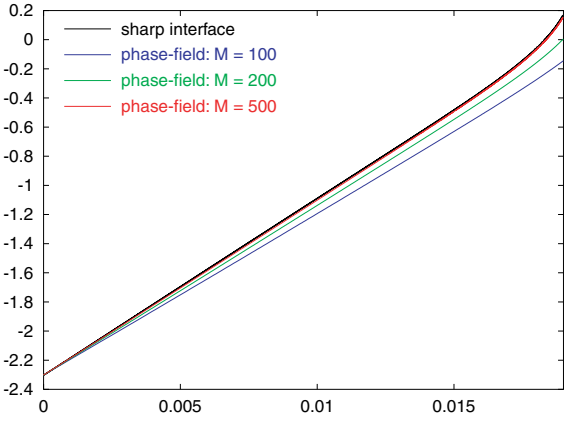

Fig. 5. Convergence of amplitude computed by phase-field model to amplitude computed by sharp interface for increasing M.

Fig. 6 shows the approximation of the result of a sharp interface simulation of (4.33) by levelsets of the phase-field function ϕ computed as a solution of the system (2.6) and (2.7) with $\psi_0 = 1$, $M = 1$ and $D = 16$ at different times. Again the algorithm in [60] is used for the sharp interface solution. In Fig. 7, the convergence

Table 1
Convergence of growthrate computed by phase-field model for increasing M

	Analytic	Sharp interface	$M = 500$	$M = 200$	$M = 100$
Growthrate	121.92	121.45	120.17	116.41	110.69

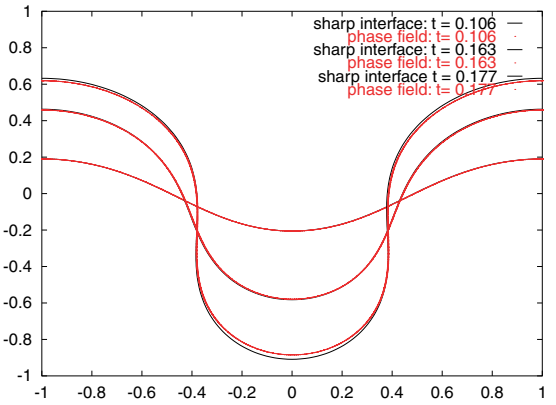

Fig. 6. Sharp interface versus phase-field at various timesteps, $D = 16$.

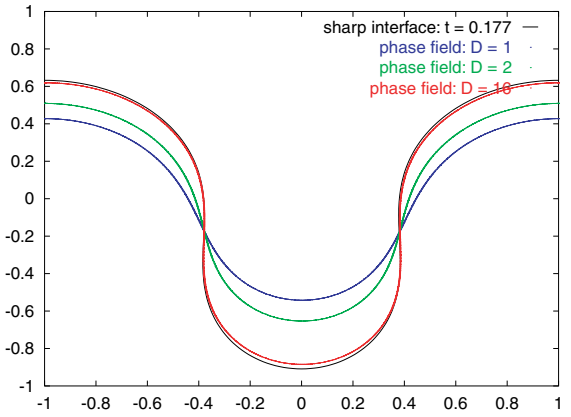

Fig. 7. Convergence of levelsets of phase-field model to sharp interface for increasing D.

of the levelsets resulting from phase-field computations with increasing D to the sharp interface solution for a selected time is shown. Fig. 8 shows the convergence of the logarithm of the amplitudes for increasing parameter D to the result of the sharp interface computation. Table 2 shows the growthrates obtained from the linear fits of the curves in Fig. 8 (fit interval [0,0.05]).

For both extreme cases the viscous Cahn–Hilliard equation shows excellent agreement with the sharp interface results and the theoretically predicted growthrates. As a consequence the viscous Cahn–Hilliard equation can be assumed to be valid in the whole parameter range going from surface diffusion to attachment-detachment dominated evolution.

4.2. Anisotropic surface evolution

As a second example we analyze various anisotropies in the viscous Cahn–Hilliard equation without elasticity. We consider a weak anisotropy in ψ_0 and a strong anisotropy in M. The modifications of the described numerical algorithm are straight forward. All additional nonlinear term are treated explicitly, meaning n is

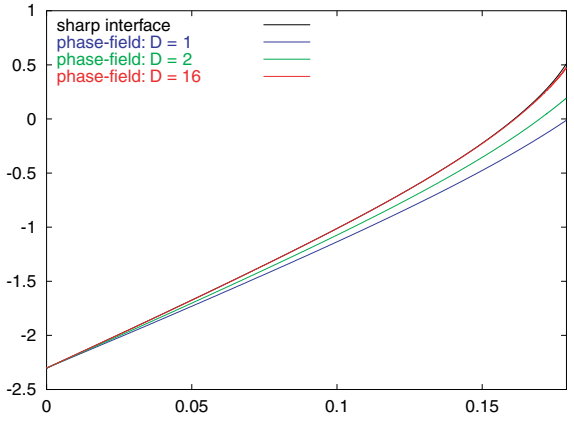

Fig. 8. Convergence of amplitude computed by phase-field model to amplitude computed by sharp interface for increasing D.

Table 2
Convergence of growthrate computed by phase-field model for increasing D

	Analytic	Sharp interface	$D = 16$	$D = 2$	$D = 1$
Growthrate	12.35	12.58	12.52	11.97	11.41

computed by $n = -\frac{\nabla\phi^{(m)}}{|\nabla\phi^{(m)}|}$. Therefore only the weighting factors in the definition of the mass and stiffness matrices $\boldsymbol{M}^3$, $\boldsymbol{A}^1$, $\boldsymbol{A}^2$ and the right hand side vector $\boldsymbol{J}$ have to be modified, see Section 3.

We first use an anisotropy function $\psi_0(n)$ of the form

$$\psi_0(n) = 1 + \epsilon_4 \sum_{i=1}^{d} n_i^4, \tag{4.35}$$

with dimension d and $\epsilon_4 = 0.3$, providing $\psi_0(\mathbf{n})\mathbf{P} + \frac{\partial^2\psi_0(\mathbf{n})}{\partial\mathbf{n}^2}$ to be positive definite. Figs. 9 and 10 show the convergence of a closed curve or surface to its Wulff shape in two and three dimensions, respectively. We solve Eqs. (2.10) and (2.11) with $D = 1$, $M = 1$ and $\psi_1 = 1$. The initial condition is a circle or a sphere, respectively.

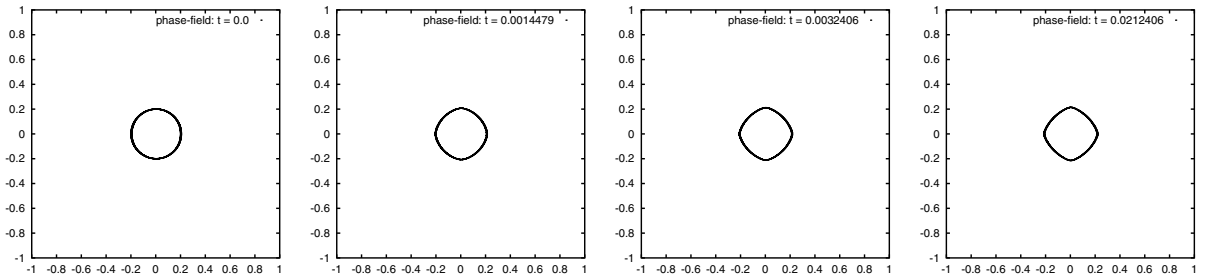

Fig. 9. Evolution of levelset $\phi = 0.5$ towards the Wulff shape in two dimensions.

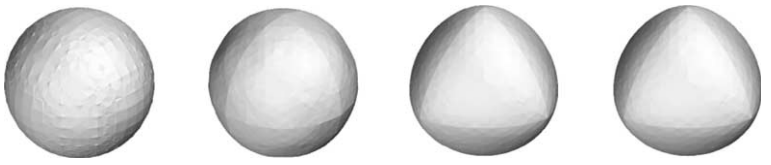

Fig. 10. Evolution of levelset $\phi = 0.5$ towards the Wulff shape in three dimensions.

Applying this anisotropy to a flat interface, does not have any influence. Because all orientations are allowed, a flat interface with $K = 0$ is a minimizer of the surface energy. Therefore, an initially flat interface will remain flat.

We now account for an anisotropy in the kinetic coefficient $M(n)$

$$M(n) = 1 - \epsilon_5 + 2\epsilon_5 \tanh\left\{k\left(\sqrt{d} - \sum_{i=1}^{d} |n_i|\right) \Big/ \left(1 - \sum_{i=1}^{d} n_i^4\right)\right\} \tag{4.36}$$

with $k = 50$ and $\epsilon_5 = 0.9$. Figs. 11 and 12 show the convergence of a closed curve or surface to its kinetic Wulff shape in two and three dimensions, respectively.

We solve Eqs. (2.10) and (2.11) with $D = 1$ and $\psi_1 = 1$ and an additional deposition flux

$$\epsilon^{-1}\tilde{j} = -\epsilon^{-1}\frac{1}{\gamma(n)} VB(\phi)\mathscr{R}\frac{\partial_z \phi}{|\nabla \phi|}$$

in Eq. (2.10) with $V = 10$. The initial condition is again a circle or a sphere, respectively. Applying this anisotropy to a flat interface still does not lead to formation of faceted structures. The flat interface remains stable.

4.3. Coupled system in three dimensions

Now we solve the visous Cahn–Hilliard equation with elasticity in the anisotropic case in the domain $\Omega = (-400, 400)^3$. The anisotropy function $\psi_0(n)$ as in (4.35) with $\epsilon_4 = 0.3$ is used as well as the kinetic coefficient $M(n)$ as in (4.36) with $k = 50$ and $\epsilon_5 = 0.9$.

The parameters for the elasticity problem are as follows: $\lambda = 3.24 \times 10^4$, $\mu = 3.48 \times 10^4$, $F = 0.008$, which corresponds to $Si_{0.82}Ge_{0.18}$, see [21] (adjusted to the model introduced in Section 2). Further parameters used in the simulations are $D = 2.56 \times 10^{10}$, $V = 1$, $\psi_1 = 1$, $\epsilon = 40$. Fig. 13 shows the evolution of an initially flat interface in the anisotropic situation.

The competition between surface and elastic energies leads to the formation of nanomounds. Faceted mounds can be observed. The faceting here results from the anisotropic kinetic coefficient. The instability however is only due to the elastic misfit. Detailed parameter studies addressing the influence of the different processes still has to be done before the simulational results can be compared with [21–23] or experiments.

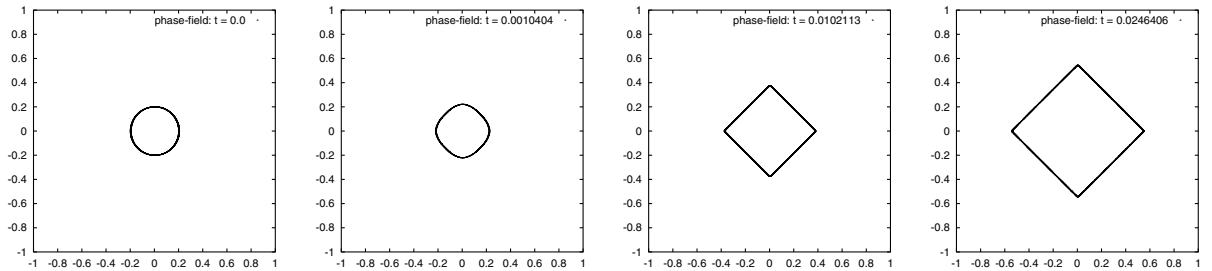

Fig. 11. Evolution of levelset $\phi = 0.5$ towards the kinetic Wulff shape in two dimensions.

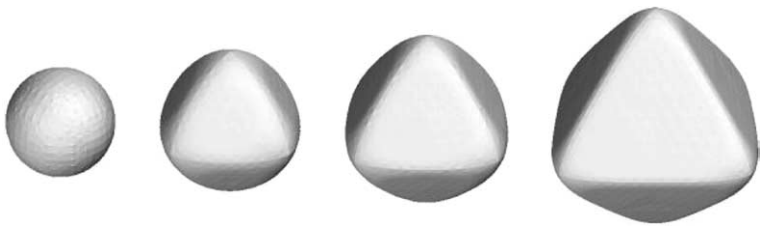

Fig. 12. Evolution of levelset $\phi = 0.5$ towards the kinetic Wulff shape in three dimensions.

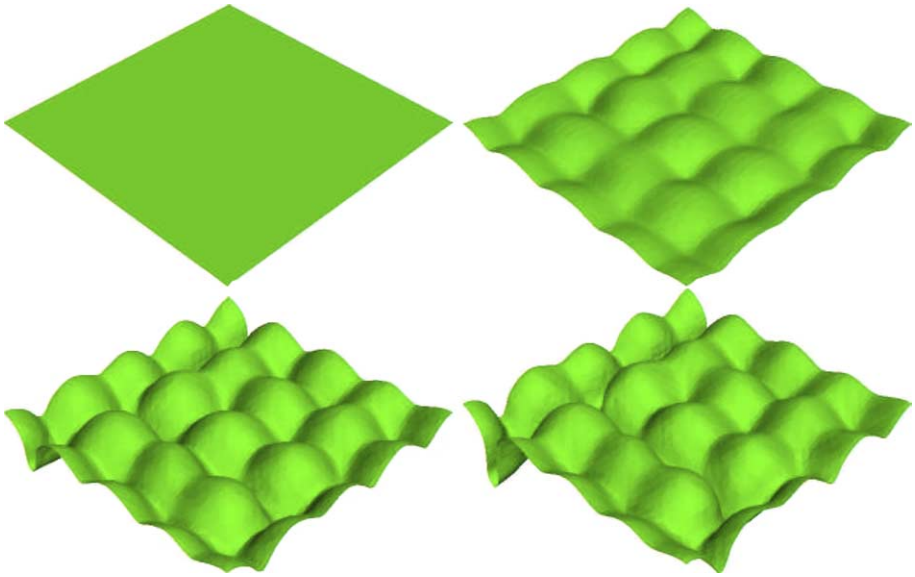

Fig. 13. Evolution of levelset $\phi = 0.5$ under the influence of elasticity, deposition flux, anisotropic surface free energy and anisotropic kinetic coefficient.

Qualitatively however they are in good agreement and demonstrate the validity of phase-field models to simulate surface evolution.

5. Conclusion

A connection between sharp interface models for anisotropic surface evolution and its diffuse interface counterpart is given. A deposition flux and elastic stress are introduced in the diffuse interface model in order to model self-organization processes in heteroepitaxial growth. The nonlinear system of equations is solved by adaptive finite elements in three dimensions. The influence of anisotropies in the surface free energy density and the kinetic coefficient on the surface evolution have been addressed.

Coming back to the different processes which can lead to self organization described in the introduction (see Fig. 1) only the evolution due to elastic misfit has been addressed in the simulations. To model the spinodal decomposition into facetted structures resulting from strong surface anisotropies the proposed sixth order system (2.12) and (2.13) has to be solved. How to incorporate mound formation resulting from kinetic fluxes resulting from step-edge barriers in a three-dimensional model is still open.

Acknowledgments

The work was partially done while one of the authors A.V. was visiting the Institute for Mathematical Sciences, National University of Singapore in 2004. The visit was supported by the institute. A.R. was supported through SPP 1095 of DFG. We thank M. Burger for pointing out the connection between Eqs. (2.1) and (2.4), (2.5) and S.J. Watson for stimulating discussions on curvature regularized geometric evolution laws.

Appendix A. Asymptotic analysis in two-dimensions

We provide a matched asymptotic analysis to show the formal convergence of:

$$\partial_t \phi = \nabla \cdot (\tilde{D}(n)\epsilon^{-1} B(\phi)\nabla w), \tag{A.1}$$

$$g(\phi)w = (-\epsilon\nabla \cdot (\gamma^2(n)\nabla\phi + \gamma(n)|\nabla\phi|^2 \nabla_{\nabla\phi}\gamma(n)) + \epsilon^{-1}G'(\phi)) + \epsilon^{-1}\frac{1}{\tilde{M}(n)}\partial_t\phi \tag{A.2}$$

for $\epsilon \to 0$ to

$$v = \partial_s \cdot (D(\mathbf{n})\partial_s w), \tag{A.3}$$

$$w = (\tilde{\psi}_0(\theta) + \tilde{\psi}_0''(\theta))K + \frac{1}{M(\mathbf{n})}v = \psi_1(\tilde{\gamma}(\theta) + \tilde{\gamma}''(\theta))K + \frac{1}{M(\mathbf{n})}v \tag{A.4}$$

with $\theta = \theta(n)$. This is the two-dimensional counterpart of Eqs. (2.8) and (2.9), with anisotropy function

$$\tilde{\gamma}(\theta) = \gamma \circ h(\theta),$$

where $h(\theta) = (\cos(\theta), \sin(\theta)) = \mathbf{n}$. This relation allows to rewrite Eq. (A.2) as

$$g(\phi)w = -\epsilon\nabla \cdot (\gamma^2(n)\nabla\phi + \gamma(n)\tilde{\gamma}'(\theta)(-\partial_y\phi, \partial_x\phi)) + \epsilon^{-1}G'(\phi) + \epsilon\frac{1}{\tilde{M}(n)}\partial_t\phi. \tag{A.5}$$

A.1. New coordinates and useful expansions

New coordinates are established in a neighborhood of the interface $\Gamma(t)$. To this end $r = r(x,y,t;\epsilon)$ is defined as the signed distance of (x,y) from $\Gamma(t;\epsilon)$, where $r < 0$, if (x,y) is in the film and $r > 0$ if (x,y) is in the vapor. The curve Γ then can be parametrized with respect to arclength s by

$$\mathbf{c} = \mathbf{c}(\cdot, t; \epsilon) : I \subset \mathbb{R} \to \Gamma(t;\epsilon), \quad I := [0, L(\Gamma)],$$

where $L(\Gamma)$ denotes the length of Γ. Let $\boldsymbol{\tau} = \boldsymbol{\tau}(s,t;\epsilon)$ and $\mathbf{n} = \mathbf{n}(s,t;\epsilon)$ denote the tangent and the normal. Then for $0 < \rho \ll 1$ there exists a neighborhood

$$U(t;\epsilon) = \{(x_1, x_2) \in \Omega : |r(x,y,t;\epsilon)| < \rho\} \tag{A.6}$$

of $\Gamma(t;\epsilon)$ such that one can write $(x,y) = c(s,t;\epsilon) + r(x,y,t;\epsilon)\mathbf{n}(s,t;\epsilon)$ for $(x,y) \in U(t;\epsilon)$. Now one transforms w and ϕ to the new coordinate system:

$$\hat{w}(r,s,t;\epsilon) := w(\mathbf{c}(s,t;\epsilon) + r\mathbf{n}(s,t;\epsilon), t;\epsilon), \qquad (x,y) \in U(t;\epsilon),$$
$$\hat{\phi}(r,s,t;\epsilon) := \phi(\mathbf{c}(s,t;\epsilon) + r\mathbf{n}(s,t;\epsilon), t;\epsilon), \qquad (x,y) \in U(t;\epsilon).$$

Furthermore a stretched variable is introduced $z := \frac{r}{\epsilon}$, and one defines

$$W(z,s,t;\epsilon) := \hat{w}(r,s,t;\epsilon),$$
$$\Phi(z,s,t;\epsilon) := \hat{\phi}(r,s,t;\epsilon).$$

In addition the following Taylor expansion approximations for small ϵ are assumed to be valid

$$w(x,y,t;\epsilon) = w_0(x,y,t) + \epsilon w_1(x,y,t) + \cdots, \tag{A.7}$$
$$\hat{w}(r,s,t;\epsilon) = \hat{w}_0(r,s,t) + \epsilon\hat{w}_1(r,s,t) + \cdots, \tag{A.8}$$
$$W(z,s,t;\epsilon) = W_0(z,s,t) + \epsilon W_1(z,s,t) + \cdots, \tag{A.9}$$
$$\phi(x,y,t;\epsilon) = \phi_0(x,y,t) + \epsilon\phi_1(x,y,t) + \cdots, \tag{A.10}$$
$$\hat{\phi}(r,s,t;\epsilon) = \hat{\phi}_0(r,s,t) + \epsilon\hat{\phi}_1(r,s,t) + \cdots, \tag{A.11}$$
$$\Phi(z,s,t;\epsilon) = \Phi_0(z,s,t) + \epsilon\Phi_1(z,s,t) + \cdots, \tag{A.12}$$

for which (A.7), (A.8) and (A.10), (A.11) are called outer expansions while (A.9) and (A.12) are called inner expansions. It is assumed that these hold simultaneously in some overlapping region and represent the same functions, which yields the matching conditions

$$\lim_{r\to\pm 0} \hat{w}_0(r,s,t) = \lim_{z\to\pm\infty} W_0(z,s,t), \tag{A.13}$$
$$\lim_{r\to\pm 0} \hat{\phi}_0(r,s,t) = \lim_{z\to\pm\infty} \Phi_0(z,s,t). \tag{A.14}$$

Let $v = v(s,t;\epsilon)$ and $K = K(s,t;\epsilon)$ denote the normal velocity and the curvature. Using

$$\partial_s \boldsymbol{\tau} = -K\mathbf{n}, \quad \partial_s \mathbf{n} = K\boldsymbol{\tau} \tag{A.15}$$

the transform of the derivatives into the new coordinates (r,s) lead

$$\partial_s \hat{\phi} = \nabla\phi \cdot (\partial_s \mathbf{c} + r\partial_s \mathbf{n}) = \nabla\phi \cdot (\partial_s \mathbf{c} + rK\partial_s \mathbf{c}) = (1 + rK)\nabla\phi \cdot \boldsymbol{\tau},$$

which yields

$$\nabla\phi \cdot \boldsymbol{\tau} = (1 + rK)^{-1}\partial_s \hat{\phi}. \tag{A.16}$$

Furthermore we get

$$\partial_r \hat{\phi} = \nabla\phi \cdot \mathbf{n} \tag{A.17}$$

as well as

$$\partial_r \hat{\phi}\partial_t r + \partial_s \hat{\phi}\partial_t s + \partial_t \hat{\phi} = \partial_t \phi + \nabla\phi \cdot (\partial_s \mathbf{c}\partial_t s + \partial_t \mathbf{c} + \partial_t r\mathbf{n} + r\partial_s \mathbf{n}\partial_t s + r\partial_t \mathbf{n})$$

which leads by using (A.16) and (A.17) to

$$\begin{aligned}
\partial_t \phi &= \partial_r \hat{\phi}\partial_t r + \partial_s \hat{\phi}\partial_t s + \partial_t \hat{\phi} - \nabla\phi \cdot (\partial_t s\boldsymbol{\tau} + (\partial_t \mathbf{c} \cdot \mathbf{n})\mathbf{n} + (\partial_t \mathbf{c} \cdot \boldsymbol{\tau})\boldsymbol{\tau} + \partial_t r\mathbf{n} + rK\partial_t s\boldsymbol{\tau} + r\partial_t \mathbf{n}) \\
&= \partial_r \hat{\phi}\partial_t r + \partial_s \hat{\phi}\partial_t s + \partial_t \hat{\phi} - \nabla\phi \cdot (\partial_t s(1 + rK)\boldsymbol{\tau} + v\mathbf{n} + (\partial_t \mathbf{c} \cdot \boldsymbol{\tau})\boldsymbol{\tau} + \partial_t r\mathbf{n} + r\partial_t \mathbf{n}) \\
&= \partial_r \hat{\phi}\partial_t r + \partial_s \hat{\phi}\partial_t s + \partial_t \hat{\phi} - \partial_s \hat{\phi}\partial_t s - v\partial_r \hat{\phi} - \partial_t r\partial_r \hat{\phi} - \nabla\phi \cdot ((\partial_t \mathbf{c} \cdot \boldsymbol{\tau})\boldsymbol{\tau} + r\partial_t \mathbf{n}) \\
&= \partial_t \hat{\phi} - v\partial_r \hat{\phi} - (1 + rK)^{-1}\partial_s \hat{\phi}(\partial_t \mathbf{c} + r\partial_t \mathbf{n}) \cdot \boldsymbol{\tau}.
\end{aligned} \tag{A.18}$$

One can express the gradient of ϕ as

$$\nabla\phi = (\nabla\phi \cdot \boldsymbol{\tau})\boldsymbol{\tau} + (\nabla\phi \cdot \mathbf{n})\mathbf{n} = \partial_r \hat{\phi}\mathbf{n} + (1 + rK)^{-1}\partial_s \hat{\phi}\boldsymbol{\tau} \tag{A.19}$$

and compute for the divergence of a vector field j

$$\begin{aligned}
\nabla \cdot j &= \partial_r \hat{j} \cdot \mathbf{n} + (1 + rK)^{-1}\partial_s \hat{j} \cdot \boldsymbol{\tau} = \partial_r(\hat{j} \cdot \mathbf{n}) + (1 + rK)^{-1}(\partial_s(\hat{j} \cdot \boldsymbol{\tau}) - \hat{j} \cdot \partial_s \boldsymbol{\tau}) \\
&= \partial_r(\hat{j} \cdot \mathbf{n}) + (1 + rK)^{-1}(\partial_s(\hat{j} \cdot \boldsymbol{\tau}) + K\hat{j} \cdot \mathbf{n}).
\end{aligned} \tag{A.20}$$

In the coordinate system (z,s) the corresponding expressions read

$$\partial_t \phi = -\epsilon^{-1}v\partial_z \Phi + \partial_t \Phi - (1 + \epsilon zK)^{-1}\partial_s \Phi(\partial_t \mathbf{c} + \epsilon z\partial_t \mathbf{n}) \cdot \boldsymbol{\tau}, \tag{A.21}$$

$$\nabla\phi = \epsilon^{-1}\partial_z \Phi\mathbf{n} + (1 + \epsilon zK)^{-1}\partial_s \Phi\boldsymbol{\tau}, \tag{A.22}$$

$$\nabla \cdot j = \epsilon^{-1}\partial_z(J \cdot \mathbf{n}) + (1 + \epsilon zK)^{-1}(\partial_s(J \cdot \boldsymbol{\tau}) + KJ \cdot \mathbf{n}). \tag{A.23}$$

Before we turn to analyse the outer and inner expansions we provide some useful calculations. For this purpose we expand

$$\begin{aligned}
n = -\frac{\nabla\phi}{|\nabla\phi|} &= -\frac{\partial_z \Phi\mathbf{n} + \epsilon(1 + \epsilon zK)^{-1}\partial_s \Phi\boldsymbol{\tau}}{[(\partial_z \Phi)^2 + (\epsilon(1 + \epsilon zK)^{-1}\partial_s \Phi)^2]^{1/2}} \\
&= -\frac{\partial_z \Phi_0\mathbf{n}}{|\partial_z \Phi_0|} + \epsilon\left(\frac{\partial_z \Phi_1\mathbf{n} + \partial_s \Phi_0\boldsymbol{\tau}}{|\partial_z \Phi_0|} - \frac{\partial_z \Phi_0 2\partial_z \Phi_0\partial_z \Phi_1\mathbf{n}}{2|\partial_z \Phi_0|^3}\right) + \mathrm{O}(\epsilon^2) \\
&= \mathbf{n} + \epsilon\frac{\partial_s \Phi_0}{\partial_z \Phi_0}\tau + \mathrm{O}(\epsilon^2),
\end{aligned}$$

where we already used $\partial_z \Phi_0 < 0$, see Eq. (A.27). Using this representation we can conclude $\frac{d}{d\epsilon}\gamma(n)_{|\epsilon=0} = \tilde{\gamma}'(\theta)\frac{\partial_s \Phi_0}{\partial_z \Phi_0}$. Another expansion, which will be used is

$$(-\partial_{x_2}\phi, \partial_{x_1}\phi) = \epsilon^{-1}\partial_z \Phi\boldsymbol{\tau} - (1 + \epsilon zK)^{-1}\partial_s \Phi\mathbf{n}.$$

Combining these results we obtain for

$$
\begin{aligned}
&\epsilon\nabla\cdot(\gamma^2(n)\nabla\phi+\gamma(n)\tilde{\gamma}'(\theta)(-\partial_{x_2}\phi,\partial_{x_1}\phi))\\
&\quad=\partial_z\{\gamma^2(n)\epsilon^{-1}\partial_z\Phi-\gamma(n)\tilde{\gamma}'(\theta)(1+\epsilon zK)^{-1}\partial_s\Phi\}\\
&\qquad+\epsilon(1+\epsilon zK)^{-1}K\{\gamma^2(n)\epsilon^{-1}\partial_z\Phi-\gamma(n)\tilde{\gamma}'(\theta)(1+\epsilon zK)^{-1}\partial_s\Phi\}\\
&\qquad+\epsilon(1+\epsilon zK)^{-1}\partial_s\{\gamma^2(n)(1+\epsilon zK)^{-1}\partial_s\Phi+\gamma(n)\tilde{\gamma}'(\theta)\epsilon^{-1}\partial_z\Phi\}\\
&\quad=\epsilon^{-1}\partial_z(\gamma^2(\mathbf{n})\partial_z\Phi_0)+\{\gamma^2(\mathbf{n})\partial_{zz}\Phi_1+\partial_z(2\gamma(\mathbf{n})\tilde{\gamma}'(\theta)\partial_s\Phi_0)-\gamma(\mathbf{n})\tilde{\gamma}'(\theta)\partial_{zs}\Phi_0\}\\
&\qquad+\{K\gamma^2(\mathbf{n})\partial_z\Phi_0+\partial_s(\gamma(\mathbf{n})\tilde{\gamma}'(\theta)\partial_z\Phi_0)\}+\mathrm{O(e)}\\
&\quad=\epsilon^{-1}\tilde{\gamma}^2(\theta)\partial_{zz}\Phi_0+\{\tilde{\gamma}^2(\theta)\partial_{zz}\Phi_1+2\tilde{\gamma}(\theta)\tilde{\gamma}'(\theta)\partial_{zs}\Phi_0+K\tilde{\gamma}^2(\theta)\partial_z\Phi_0\}\\
&\qquad+\{((\tilde{\gamma}'(\theta))^2+\tilde{\gamma}(\theta)\tilde{\gamma}''(\theta))K\partial_z\Phi_0\}+\mathrm{O}(\epsilon),
\end{aligned}
$$

where we have used $\gamma(\mathbf{n})=\tilde{\gamma}(\theta)$, $\partial_s\gamma(\mathbf{n})=\tilde{\gamma}'(\theta)K$ and $\partial_s\tilde{\gamma}'(\theta)=\tilde{\gamma}''(\theta)K$, which follows from

$$
\begin{aligned}
\partial_s\gamma(\mathbf{n})&=\partial_s(\gamma\circ h\circ h^{-1}\circ\mathbf{n})=\tilde{\gamma}'(\theta)\partial_s(h^{-1}\circ\mathbf{n})=\tilde{\gamma}'(\theta)\frac{1}{1+n_2^2/n_1^2}\frac{\partial_s n_2 n_1-n_2\partial_s n_1}{n_1^2}=\tilde{\gamma}'(\theta)\partial_s n_2 n_1-n_2\partial_s n_1\\
&=\tilde{\gamma}'(\theta)\partial_s n\cdot\boldsymbol{\tau}=\tilde{\gamma}'(\theta)K\boldsymbol{\tau}\cdot\boldsymbol{\tau}=\tilde{\gamma}'(\theta)K.
\end{aligned}
$$

We now turn to the outer and inner expansion of (A.1) and (A.2).

A.2. Outer expansion

By inserting the outer expansions into (A.2) we obtain:

$$G'(\phi_0)=0\Rightarrow\phi_0\in\{0,1\} \tag{A.24}$$

and

$$\lim_{r\to+0}\phi_0=0,\qquad\lim_{r\to-0}\phi_0=1. \tag{A.25}$$

A.3. Inner expansion

By inserting the inner expansions into (A.5) we obtain $\mathrm{O}(\epsilon^{-1})$ in (A.5)

$$0=\tilde{\gamma}^2(\theta)\partial_{zz}\Phi_0-G'(\Phi_0). \tag{A.26}$$

From this we get by multiplying (A.26) by $\partial_z\Phi_0$ and integrating from $-\infty$ to z

$$\tilde{\gamma}^2(\theta)(\partial_z\Phi_0)^2=2G(\Phi_0),$$

which yields

$$\partial_z\Phi_0=-\frac{\sqrt{2G(\Phi_0)}}{\tilde{\gamma}(\theta)} \tag{A.27}$$

leading to

$$\int_{-\infty}^{+\infty}(\partial_z\Phi_0)^2\,\mathrm{d}z=\frac{1}{\tilde{\gamma}(\theta)}\int_0^1\sqrt{2G(\phi)}\,\mathrm{d}\phi=\frac{1}{\tilde{\gamma}(\theta)} \tag{A.28}$$

by the concrete choice of $G=G(\phi)$. This will be used in the inner expansion in (A.1)

$$
\begin{aligned}
-\epsilon^{-1}v\partial_z\Phi=\epsilon^{-3}\partial_z(\tilde{D}(n)B(\Phi)\partial_z W)+\epsilon^{-2}K(1+\epsilon zK)^{-1}\tilde{D}(n)B(\Phi)\partial_z W\\
+\epsilon^{-1}(1+\epsilon zK)^{-1}\partial_s(\tilde{D}(n)B(\Phi)(1+\epsilon zK)^{-1}\partial_s W),
\end{aligned}
$$

which yields in $\mathrm{O}(\epsilon^{-3})$ in (A.1)

$$0=\partial_z(\tilde{D}(\mathbf{n})B(\Phi_0)\partial_z W_0).$$

From this one gets

$$\tilde{D}(\mathbf{n})B(\Phi_0)\partial_z W_0 = \text{const},$$

the constant being zero because of $\lim_{|z|\to\infty} B(\Phi_0) = 0$. So one finally arrives at

$$\partial_z W_0 = 0 \Rightarrow W_0 \equiv W_0(s,t). \tag{A.29}$$

Using (A.29) one obtains in $O(\epsilon^{-2})$ in (A.1)

$$0 = \partial_z(\tilde{D}(\mathbf{n})B(\Phi_0)\partial_z W_1).$$

As before this yields

$$\partial_z W_1 = 0. \tag{A.30}$$

Finally one makes use of (A.29) and (A.30) to obtain in $O(\epsilon^{-1})$ in (A.1)

$$-v\partial_z\Phi_0 = \partial_z(\tilde{D}(\mathbf{n})B(\Phi_0)\partial_z W_2) + \partial_s(\tilde{D}(\mathbf{n})B(\Phi_0)\partial_s W_0).$$

Integrating this equation along the z-axis one obtains

$$v = \partial_s\left(\tilde{D}(\mathbf{n})\int_{-\infty}^{+\infty} B(\Phi_0)\,\mathrm{d}z\,\partial_s W_0\right), \tag{A.31}$$

where

$$\begin{aligned}\int_{-\infty}^{+\infty} B(\Phi_0)\,\mathrm{d}z &= 36\int_{-\infty}^{+\infty}\Phi_0^2(1-\Phi_0)^2\,\mathrm{d}z = -36\int_{-\infty}^{+\infty}\frac{\Phi_0^2(1-\Phi_0)^2}{\sqrt{2G(\Phi_0)}}\tilde{\gamma}(\theta)\partial_z\Phi_0\,\mathrm{d}z = \frac{36}{6}\tilde{\gamma}(\theta)\int_0^1\phi(1-\phi)\,\mathrm{d}\phi\\ &= \frac{6\tilde{\gamma}(\theta)}{6} = \tilde{\gamma}(\theta).\end{aligned}$$

So we end up using the definition of $\tilde{D} = D/\gamma$

$$v = \partial_s(\tilde{D}(\mathbf{n})\tilde{\gamma}(\theta)\partial_s W_0) = \partial_s(D(\mathbf{n})\partial_s W_0), \tag{A.32}$$

which is Eq. (A.3). Now we turn back to (A.2) and obtain $O(\epsilon^0)$ in (A.2)

$$\begin{aligned}g(\Phi_0)W_0 = \psi_1(&-\tilde{\gamma}^2(\theta)\partial_{zz}\Phi_1 - 2\tilde{\gamma}(\theta)\tilde{\gamma}'(\theta)\partial_{zs}\Phi_0 - K\tilde{\gamma}^2(\theta)\partial_z\Phi_0 - ((\tilde{\gamma}'(\theta))^2 + \tilde{\gamma}(\theta)\tilde{\gamma}''(\theta))K\partial_z\Phi_0\\ &+ G''(\Phi_0)\Phi_1) - \frac{1}{\tilde{M}(\mathbf{n})}v\partial_z\Phi_0.\end{aligned}$$

Testing this equation with $\partial_z\Phi_0$ one gets

$$\begin{aligned}W_0\int_{-\infty}^{+\infty} g(\Phi_0)\partial_z\Phi_0\,\mathrm{d}z = \psi_1\Bigg(&-\tilde{\gamma}^2(\theta)\int_{-\infty}^{+\infty}\partial_{zz}\Phi_1\partial_z\Phi_0\,\mathrm{d}z - \tilde{\gamma}(\theta)\tilde{\gamma}'(\theta)\partial_s\int_{-\infty}^{+\infty}(\partial_z\Phi_0)^2\,\mathrm{d}z\\ &- K\tilde{\gamma}^2(\theta)\int_{-\infty}^{+\infty}(\partial_z\Phi_0)^2\,\mathrm{d}z - ((\tilde{\gamma}'(\theta))^2 + \tilde{\gamma}(\theta)\tilde{\gamma}''(\theta))K\int_{-\infty}^{+\infty}(\partial_z\Phi_0)^2\,\mathrm{d}z\\ &+ \int_{-\infty}^{+\infty} G''(\Phi_0)\Phi_1\partial_z\Phi_0\,\mathrm{d}z\Bigg) - \frac{1}{\tilde{M}(\mathbf{n})}v\int_{-\infty}^{+\infty}(\partial_z\Phi_0)^2\,\mathrm{d}z.\end{aligned}$$

We use integration by parts to obtain

$$\begin{aligned}\tilde{\gamma}^2(\theta)\int_{-\infty}^{+\infty}\partial_{zz}\Phi_1\partial_z\Phi_0\,\mathrm{d}z - \int_{-\infty}^{+\infty} G''(\Phi_0)\Phi_1\partial_z\Phi_0\,\mathrm{d}z &= \tilde{\gamma}^2(\theta)\int_{-\infty}^{+\infty}\Phi_1\partial_{zzz}\Phi_0\,\mathrm{d}z - \int_{-\infty}^{+\infty}\partial_z(G'(\Phi_0))\Phi_1\,\mathrm{d}z\\ &= \int_{-\infty}^{+\infty}\Phi_1\partial_z(\tilde{\gamma}^2(\theta)\partial_{zz}\Phi_0 - G'(\Phi_0))\,\mathrm{d}z = 0.\end{aligned}$$

Furthermore we have

$$\int_{-\infty}^{+\infty} g(\Phi_0)\partial_z\Phi_0\,\mathrm{d}z = -1,$$

which together lead to

$$W_0 = \psi_1(\tilde{\gamma}(\theta)\tilde{\gamma}'(\theta)\partial_s\frac{1}{\tilde{\gamma}(\theta)} + \tilde{\gamma}(\theta)K + ((\tilde{\gamma}'(\theta))^2 + \tilde{\gamma}(\theta)\tilde{\gamma}''(\theta))\frac{K}{\tilde{\gamma}(\theta)}) + \frac{1}{\tilde{M}(\mathbf{n})\tilde{\gamma}(\theta)}v$$

and finally to

$$\begin{aligned} W_0 &= \psi_1\left(-\frac{(\tilde{\gamma}'(\theta))^2}{\tilde{\gamma}(\theta)}K + \tilde{\gamma}(\theta)K + \frac{(\tilde{\gamma}'(\theta))^2}{\tilde{\gamma}(\theta)}K + \tilde{\gamma}''(\theta)K\right) + \frac{1}{\tilde{M}(\mathbf{n})\tilde{\gamma}(\theta)}v \\ &= \psi_1(\tilde{\gamma}(\theta) + \tilde{\gamma}''(\theta))K + \frac{1}{\tilde{M}(\mathbf{n})\tilde{\gamma}(\theta)}v. \end{aligned} \tag{A.33}$$

Together with the definition of $\tilde{M} = M/\gamma$ this is Eq. (A.4), which completes the analysis. Finally we would like to remark that the incorporation of the anisotropy γ in the diffusion coefficient $\tilde{D}$ and the mobility function $\tilde{M}$ naturally follows from the asymptotic analysis. If we in addition would consider a deposition flux in (A.1), also the flux has to be changed to $\tilde{j} = j/\gamma$.

References

[1] R. Asaro, W.A. Tiller, Interface morphology development during stress-corrosion cracking. 1. via surface diffusion, Metall. Trans. 2 (1972) 1789.
[2] M.A. Grinfeld, Instability of interface between nonhydrostatically stressed elastic body and melts, Doklady Akademii Nauk SSSR 290 (1986) 1358–1363.
[3] D.J. Srolovitz, On the stability of surfaces of stressed solids, Acta Metall. 37 (1989) 621–625.
[4] H.J. Gao, W.D. Nix, Surface roughening of heteroepitaxial thin films, Ann. Rev. Mater. Sci. 29 (1999) 179–209.
[5] R.M. Tromp, F.M. Ross, M.C. Reuter, Instability driven SiGe island growth, Phys. Rev. Lett. 84 (2000) 4641–4644.
[6] F. Liu, H. Metiu, Dynamics of phase-separation of crystal-surfaces, Phys. Rev. B 48 (1993) 5808–5817.
[7] J. Stewart, N. Goldenfeld, Spinodal decomposition of a crystal-surface, Phys. Rev. B 46 (1992) 6505–6512.
[8] A.A. Golovin, S.H. Davis, A.A. Nepomnyashchy, A convective Cahn–Hilliard model for the formation of facets and corners in crystal growth, Physica D 118 (1998) 202–230.
[9] T.V. Savine, A.A. Golovin, S.H. Davis, A.A. Nepomnyashchy, P.W. Voorhees, Faceting of a growing crystal surface by surface diffusion, Phys. Rev. E 67 (2003) 021606.
[10] S.J. Watson, F. Otto, B.Y. Rubinstein, S.H. Davis, Coarsening dynamics of the convective Cahn–Hilliard equation, Physica D 178 (2003) 127–148.
[11] F. Haußer, A. Voigt, Facet formation and coarsening modeled by a geometric evolution law for epitaxial growth, J. Cryst. Growth 275 (2005) e47–e51.
[12] M. Burger, Numerical simulation of anisotropic surface diffusion with curvature-dependent energy, J. Comput. Phys. 52 (2005) 311–337.
[13] M.E. Gurtin, M.E. Jabbour, Interface evolution in three dimensions with curvature-dependent energy and surface diffusion: Interface-controlled evolution, phase transitions, epitaxial growth of elastic films, Arch. Ration. Mech. Anal. 163 (2002) 171–208.
[14] J. Villain, Continuum models of crystal growth from atomic-beams with and without desorption, J. Phys. 1 (1991) 19–42.
[15] M. Siegert, M. Plischke, Slope selection and coarsening in molecular-beam epitaxy, Phys. Rev. Lett. 78 (1994) 3705–3708.
[16] C. Duport, P. Politi, J. Villain, Growth instabilities induced by elasticity in a vicinal surface, J. Phys. I 5 (1995) 1317–1350.
[17] Y. Xiang, Derivation of a continuum model for epitaxial growth with elasticity on vicinal surface, SIAM J. Appl. Math. 63 (2002) 241–258.
[18] Y. Xiang, W. E, Misfit elastic energy and a continuum model for epitaxial growth with elasticity on vicinal surfaces, Phys. Rev. B 69 (2004) 035409.
[19] V.B. Shenoy, L.B. Freund, A continuum description of the energetics and evolution of stepped surfaces in strained nanostructures, J. Mech. Phys. Solids 50 (2002) 1817–1841.
[20] E. Fried, M.E. Gurtin, A unified treatment of evolving interfaces accounting for small deformations and atomic transport with emphasis on grain-boundaries and epitaxy, Adv. Appl. Mech. 40 (2005).
[21] Y.W. Zhang, A.F. Bower, Numerical simulations of island formation in a coherent strained epitaxial thin film system, J. Mech. Phys. Solids 47 (1999) 2273–2297.
[22] Y.W. Zhang, A.F. Bower, P. Liu, Morphological evolution driven by strain induced surface diffusion, Thin Solid Films 424 (2003) 9–14.
[23] A. Ramasubramaniam, V.B. Shenoy, Three-dimensional simulations of self-assembly of hut-shaped Si–Ge quantum dots, J. Appl. Phys. 95 (2004) 7813–7824.

[24] J.W. Cahn, J.E. Taylor, Surface motion by surface-diffusion, Acta Metall. 42 (1994) 1045–1063.
[25] W.W. Mullins, Theory of thermal grooving, J. Appl. Phys. 28 (1957) 333–339.
[26] J.W. Cahn, C.M. Elliott, A. Novick-Cohen, The Cahn–Hilliard equation with a concentration dependent mobility: motion by minus the Laplacian of the mean curvature, Eur. J. Appl. Math. 7 (1996) 287–301.
[27] C.M. Elliott, H. Garcke, On the Cahn–Hilliard equation with degenerate mobility, SIAM J. Math. Anal. 27 (1996) 404–423.
[28] A. Karma, W.J. Rappel, Quantitative phase-field modeling of dendritic growth in two and three dimensions, Phys. Rev. E 57 (1998) 4323–4349.
[29] J.W. Cahn, J.E. Taylor, Linking anisotropic sharp and diffuse surface motion laws via gradient flows, J. Stat. Phy. 77 (1994) 183–197.
[30] G.B. McFadden, A.A. Wheeler, R.J. Braun, S.R. Coriell, R.F. Sekerka, Phase-field models for anisotropic interfaces, Phys. Rev. E 48 (1993) 2016–2024.
[31] T. Uehara, R.F. Sekerka, Phase field simulations of faceted growth for strong anisotropy of kinetic coefficient, J. Cryst. Growth 254 (2003) 251–261.
[32] R. Sekerka, Analytical criteria for missing orientations on three-dimensional equilibrium shapes, J. Cryst. Growth (2005).
[33] S. Angenent, M.E. Gurtin, Multiphase thermomechanics with interfacial structure. ii. evolution of an isothermal interface, Arch. Ration. Mech. Anal. 108 (1989) 323–391.
[34] J.J. Eggleston, G.B. McFadden, P.W. Voorhees, A phase-field model for highly anisotropic interfacial energy, Physica D 150 (2001) 91–103.
[35] A. DiCarlo, M.E. Gurtin, P. Podio-Guidugli, A regularized equation for anisotropic motion-by-curvate, SIAM J. Appl. Math. 52 (1992) 1111–1119.
[36] A. Pimpinelli, J. Villain, Physics of Crystal Growth, Cambridge University Press, 1998.
[37] T. Michely, J. Krug, Islands, Mounds and Atoms, Springer, Berlin, 2004, Patterns and Processes in Crystal Growth Far from Equilibrium.
[38] Q. Du, C. Liu, X. Wang, A phase-field formulation of the Willmore problem, Nonlinearity 18 (2005) 1249–1267.
[39] W.H. Yang, D.J. Srolovitz, Crack-like surface instabilities in stressed solids, Phys. Rev. Lett. 71 (1993) 1593–1596.
[40] W.H. Yang, D.J. Srolovitz, Surface-morphology evolution in stressed solids – surface-diffusion controlled crack initiation, J. Mech. Phys. Solids 42 (1994) 1551–1574.
[41] B.J. Spencer, D.I. Meiron, Nonlinear evolution of the stress-driven morphological instability in a 2-dimensional semiinfinite solid, Acta Metall. Mater. 42 (1994) 3629–3641.
[42] F. Larché, J.W. Cahn, A linear theory of thermochemical equilibrium of solids under stress, Acta Metall. 21 (1973) 1051–1063.
[43] J. Muller, M. Grant, Model of surface instabilities induced by stress, Phys. Rev. Lett. 82 (1999) 1736–1739.
[44] K. Kassner, C. Misbah, A phase-field approach for stress-induced instabilities, Europhys. Lett. 46 (1999) 217–223.
[45] Y.U. Wang, Y.M. Jin, A.G. Khachaturyan, Phase field microelasticity modeling of surface instability of heteroepitaxial thin films, Acta Mater. 52 (2004) 81–92.
[46] P.H. Leo, J.S. Lowengrub, H.J. Jou, A diffuse interface model for microstructural evolution in elastically stressed films, Acta Mater. 46 (1998) 2113–2130.
[47] H. Garcke, S. Maier-Paape, U. Weikard, Spinodal decomposition in the presence of elastic interactions, in: Geometric Analysis and Nonlinear Partial Differential Equations, Springer, Berlin, 2003, pp. 603–635.
[48] B.J. Spencer, Asymptotic derivation of the glues-wetting layer model and contact angle condition for Stranski–Krastanow islands, Phys. Rev. B 59 (1999) 2557–2567.
[49] V.A. Shchukin, D. Bimberg, Spontaneous ordering of nanostructures on crystal surfaces, Rev. Mod. Phys. 71 (1999) 1125–1171.
[50] F. Leonard, M. Laradji, R.C. Desai, Phase separation in heteroepitaxial thin-film growth, Physica A 239 (1997) 129–136.
[51] B.J. Spencer, P.W. Voorhees, J. Tersoff, Morphological instability theory for strained alloy film growth: the effect of compositional stresses and species-dependent surface mobilities on ripple formation during epitaxial film deposition, Phys. Rev. B 64 (2001) 235318.
[52] W. Lu, Z. Suo, Dynamics of nanoscale pattern formation of an epitaxial monolayer, J. Mech. Phys. Solids 49 (2001) 1937–1950.
[53] J.J. Eggleston, P.W. Voorhees, Ordered growth of nanocrystals via a morphological instability, Appl. Phys. Lett. 80 (2002) 306–308.
[54] S.M. Wise, J.S. Lowengrub, J.S. Kim, W.C. Johnson, Efficient phase-field simulation of quantum dot formation in a strained heteroepitaxial film, Superlattice Microst. 36 (2004) 293–304.
[55] J. Barrett, H. Garcke, R. Nürnberg. in preparation.
[56] S. Vey, A. Voigt, AMDiS – adaptive multidimensional simulations: object oriented software concepts for scientific computing, WSEAS Trans. Syst. 3 (2004) 1564–1569.
[57] C. Stöcker, S. Vey, A. Voigt, AMDiS – adaptive multidimensional simulations: composite finite elements and signed distance functions, WSEAS Trans. Circuit Syst. 4 (2005) 111–116.
[58] R. Verfürth, A Review of a Posteriori Error Estimation and Adaptive Mesh-refinement Techniques, Wiley-Teubner, 1996.
[59] E. Bänsch, P. Morin, R.H. Nochetto, Surface diffusion of graphs: variational formulation, error analysis, and simulation, SIAM J. Numer. Anal. 42 (2) (2004) 773–799 (electronic).
[60] E. Bänsch, F. Haußer, O. Lakkis, B. Li, Finite element method for epitaxial growth with attachment-detachment kinetics, J. Comput. Phys. 194 (2004) 409–434.